Science Advances
AAAS

advances.sciencemag.org/cgi/content/full/6/44/eabc9174/DC1

Supplementary Materials for

K_{2P} channel C-type gating involves asymmetric selectivity filter order-disorder transitions

Marco Lolicato, Andrew M. Natale, Fayal Abderemane-Ali, David Crottès, Sara Capponi, Ramona Duman, Armin Wagner, John M. Rosenberg, Michael Grabe*, Daniel L. Minor Jr.*

*Corresponding author. Email: michael.grabe@ucsf.edu (M.G.); daniel.minor@ucsf.edu (D.L.M)

Published 30 October 2020, *Sci. Adv.* **6**, eabc9174 (2020)
DOI: 10.1126/sciadv.abc9174

The PDF file includes:

Other Supplementary Material for this manuscript includes the following:

(available at advances.sciencemag.org/cgi/content/full/6/44/eabc9174/DC1)

a

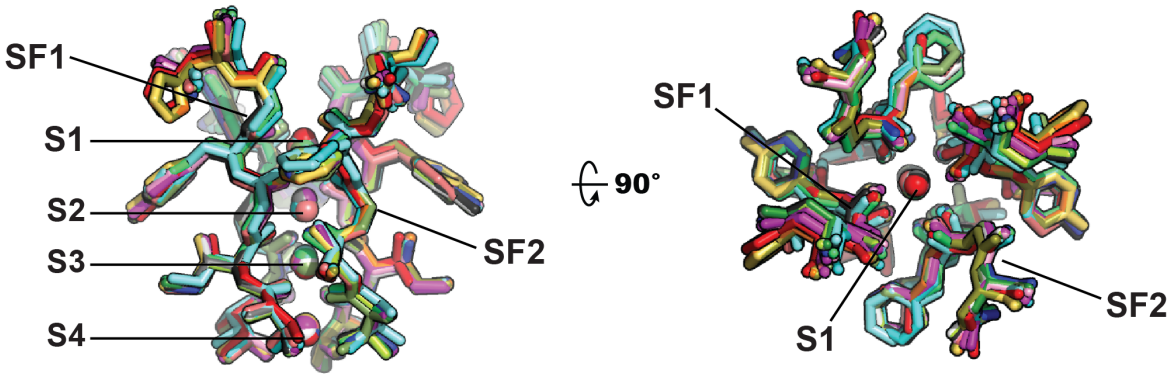

b

Structure (M4 status)	PDB code	Ion concentration	RMSD$_{C\alpha}$(Å)
K_{2P}2.1 (TREK-1) (up)	6CQ6	200 mM KCl	N.A.
K_{2P}2.1 (TREK-1):ML335(up)	6CQ8	200 mM KCl	0.25
K_{2P}2.1 (TREK-1):ML402 (up)	6CQ9	200 mM KCl	0.33
K_{2P}10.1 (TREK-2) (up)	4BW5	200 mM KCl	0.30/0.31
K_{2P}10.1 (TREK-2) (down)	4XDJ	200 mM KCl	0.33/0.33
K_{2P}10.1 (TREK-2):norfluoxitine (down)	4XDK	200 mM KCl	0.32/0.27
K_{2P}4.1 (TRAAK) (down)	3UM7	150 mM KCl*	0.55
K_{2P}4.1 (TRAAK):Fab (down)	4I9W	150 mM KCl*	0.38
K_{2P}4.1 (TRAAK):Fab (up)	4WFE	150 mM KCl*	0.38
K_{2P}4.1 (TRAAK):Fab (down)	4WFF	150 mM KCl*	0.37
K_{2P}4.1 (TRAAK):Fab (up)	4WFG	150 mM $TlNO_3$*	0.37
K_{2P}4.1 (TRAAK):Fab (up)	4WFH	150 mM $TlNO_3$*	0.39
K_{2P}4.1 (TRAAK) G124I (down)	4RUE	150 mM KCl*	0.36
K_{2P}4.1 (TRAAK) W262S (down)	4RUF	150 mM KCl*	0.38
K_{2P}1.1 (TWIK-1) (down)	3UKM	150 mM KCl	0.41/0.42
K_{2P}3.1 (TASK-1) (X-gate, down)	6RV2	200 mM KCl	0.33/0.34
K_{2P}3.1 (TASK-1) (X-gate, down)	6RV3	200 mM KCl	0.33/0.34
K_{2P}3.1 (TASK-1) (X-gate, down)	6RV4	200 mM KCl	0.34/0.35

Fig. S1 K_{2P} channel selectivity filters structure comparison. a, Superposition of the selectivity filters and permeant ions for: K_{2P}2.1 (TREK-1) (6CQ6)(*20*) (smudge), K_{2P}2.1 (TREK-1):ML335 (6CQ8)(*20*) (deep salmon), K_{2P}2.1 (TREK-1):ML402 (cyan) (6CQ9)(*20*); K_{2P}10.1 (TREK-2) (4BW5)(*21*) (pink), (4XDJ)(*21*) (magenta), (4XDK)(*21*) (purple); K_{2P}4.1 (TRAAK) (3UM7)(*22*) (aquamarine), (4I9W)(*23*) (limon), (4WFE) (forest green)(*24*), (4WFF) (white)(*24*),(4WFG) (grey)(*24*), (4WFH) (black)(*24*); K_{2P}4.1 (TRAAK) G124I (4RUE) (blue)(*25*) K_{2P}4.1 (TRAAK) W262S (4RUF) (lime green)(*25*); K_{2P}1.1 (TWIK-1) (3UKM)(*26*) (red). K_{2P}3.1 (TASK-1) (6RV2) (orange)(*43*), K_{2P}3.1 (TASK-1):BAY1000493 (6RV3) (yellow orange)(*43*), and K_{2P}3.1 (TASK-1):BAY2341237(6RV4) (olive)(*43*). SF1, SF2 and ion binding positions, S1-S4, are indicated. Ions are shown as spheres and colored according to the parent structure. **b,** K_{2P} channel structures, permeant ion concentration in crystallization conditions, and RMSD for all selectivity filter backbone atoms relative to K_{2P}2.1 (TREK-1) (6CQ6)(*20*). Structures with two RMSD values indicate

structures having chains A/B and C/D, respectively. '*' indicates samples where permeant ions were part of the protein sample buffer.

Fig. S2

Lolicato *et al.*

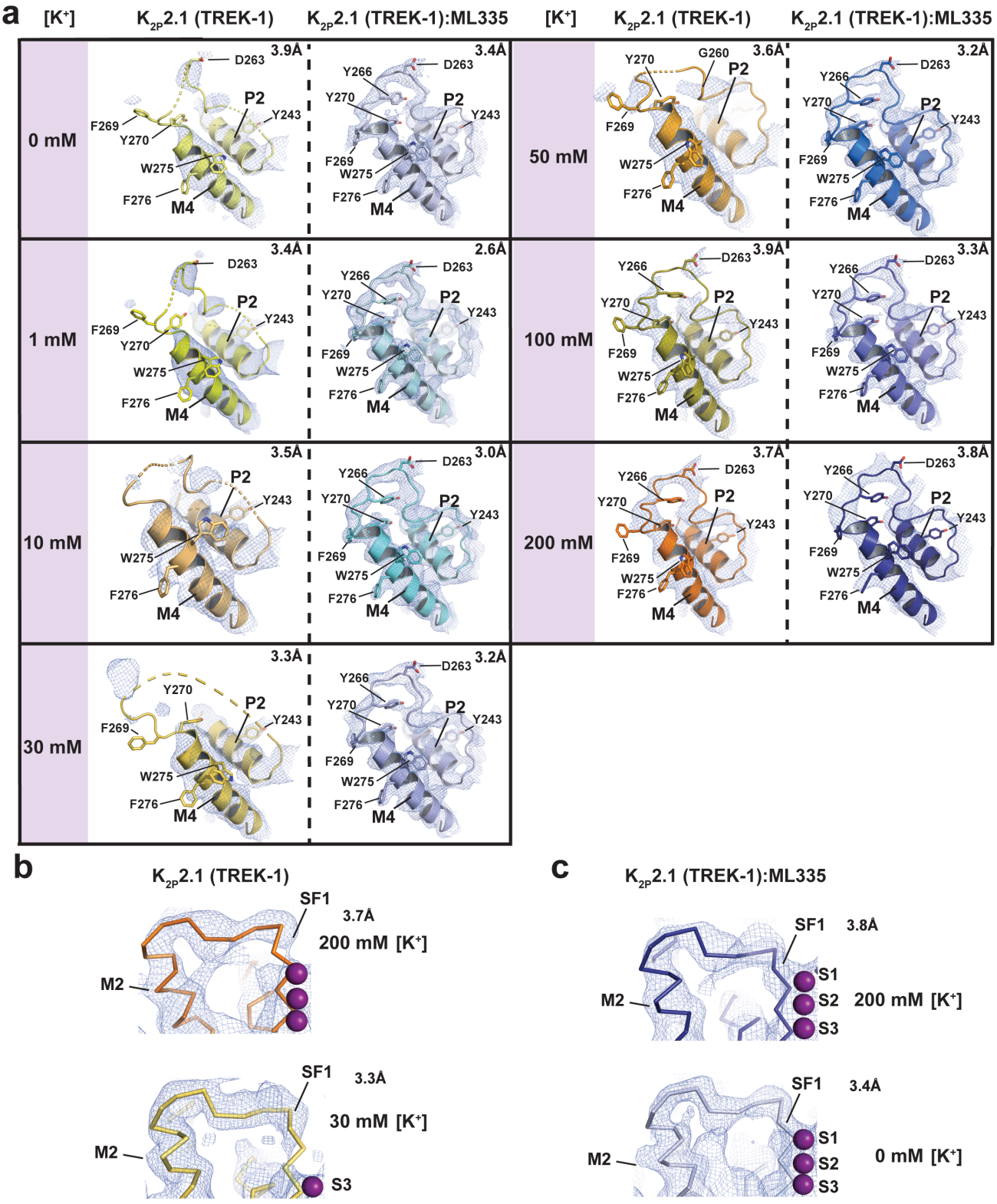

Fig. S2 K_{2P}2.1 (TREK-1) selectivity filter potassium-dependent conformational changes. a, SF2 exemplar 2Fo-Fc electron density (1σ) for K_{2P}2.1 (TREK-1) (left) and K_{2P}2.1 (TREK-1):ML335 (right) structures under 0 mM (pale yellow; blue white), 1 mM (yellow; pale cyan), 10 mM (light orange;

aquamarine) , 30 mM (yellow orange; light blue), 50 mM (bright orange; marine), 100 mM (olive; slate), and 200 mM (orange; deep blue) [K^+]. Dashed lines indicate regions of disorder. Resolution and select residues and channel elements are indicated. **b,** and **c** Exemplar SF1-M2 loop density for **b,** $K_{2P}2.1$ (TREK-1) under 30 mM (yellow orange) and 200 mM (orange) [K^+] and c, $K_{2P}2.1$ (TREK-1):ML335 under 0 mM (blue white) and 200 mM (deep blue) [K^+]. Examples show that the highest resolution low [K^+] structure, 30 mM [K^+], has a well-defined SF1-M2 loop, contrasting the poorly resolved SF2-M4 loop. Hence, the structural changes are local and not related to resolution.

Fig. S3

Lolicato *et al.*

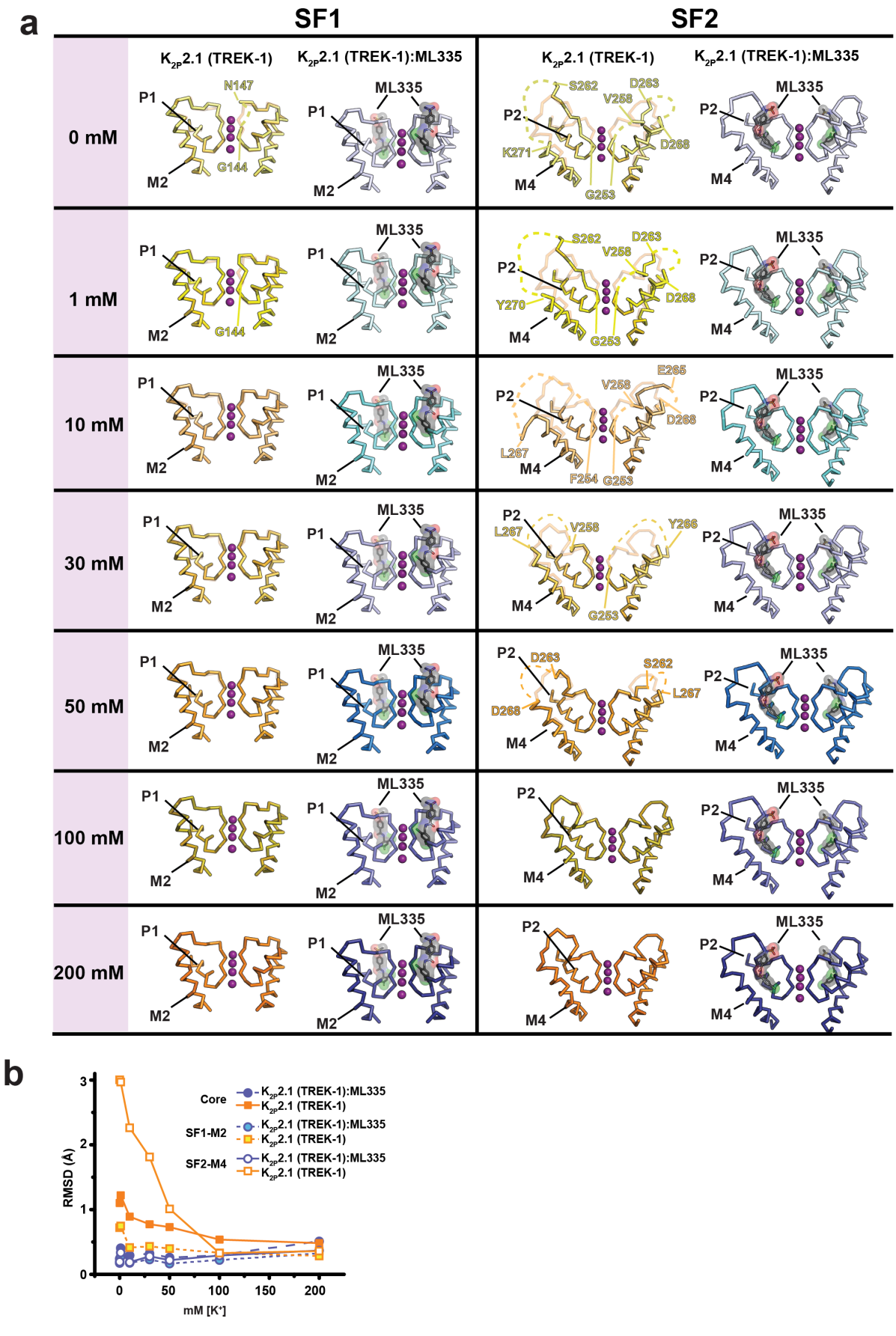

Fig. S3 Selectivity filter structural changes as a function of potassium concentration. a, $K_{2P}2.1$ (TREK-1) and the $K_{2P}2.1$ (TREK-1):ML335 complex SF1 and SF2 structures determined at the indicated potassium concentrations: 0 mM (pale yellow; blue white), 1 mM (yellow; pale cyan), 10 mM (light orange; aquamarine) , 30 mM (yellow orange; light blue), 50 mM (bright orange; marine), 100 mM (olive; slate), and 200 mM [K^+] (orange; deep blue). $K_{2P}2.1$ (TREK-1) panels show an overlay with the 200 mM [K^+] $K_{2P}2.1$ (TREK-1) structure in lighter shading. Labels indicate the last visible residue at points where the chain becomes disordered. Potassium ions from the 200 mM [K^+] structures are shown in all panels as a reference. **b,** $K_{2P}2.1$ (TREK-1) and $K_{2P}2.1$ (TREK-1):ML335 complex $RMSD_{C\alpha}$ as a function of [K^+]. Structures are compared to $K_{2P}2.1$ (TREK-1) in 200 mM [K^+] (PDB:6CQ6) and $K_{2P}2.1$ (TREK-1):ML335 complex in 200 mM [K^+] (PDB:6CQ8), respectively. Channel elements are grouped as follows: Core: residues 50-146, 153-255, 269-311; SF1-M2: residues 142-188; and SF2-M4: residues 251-295.

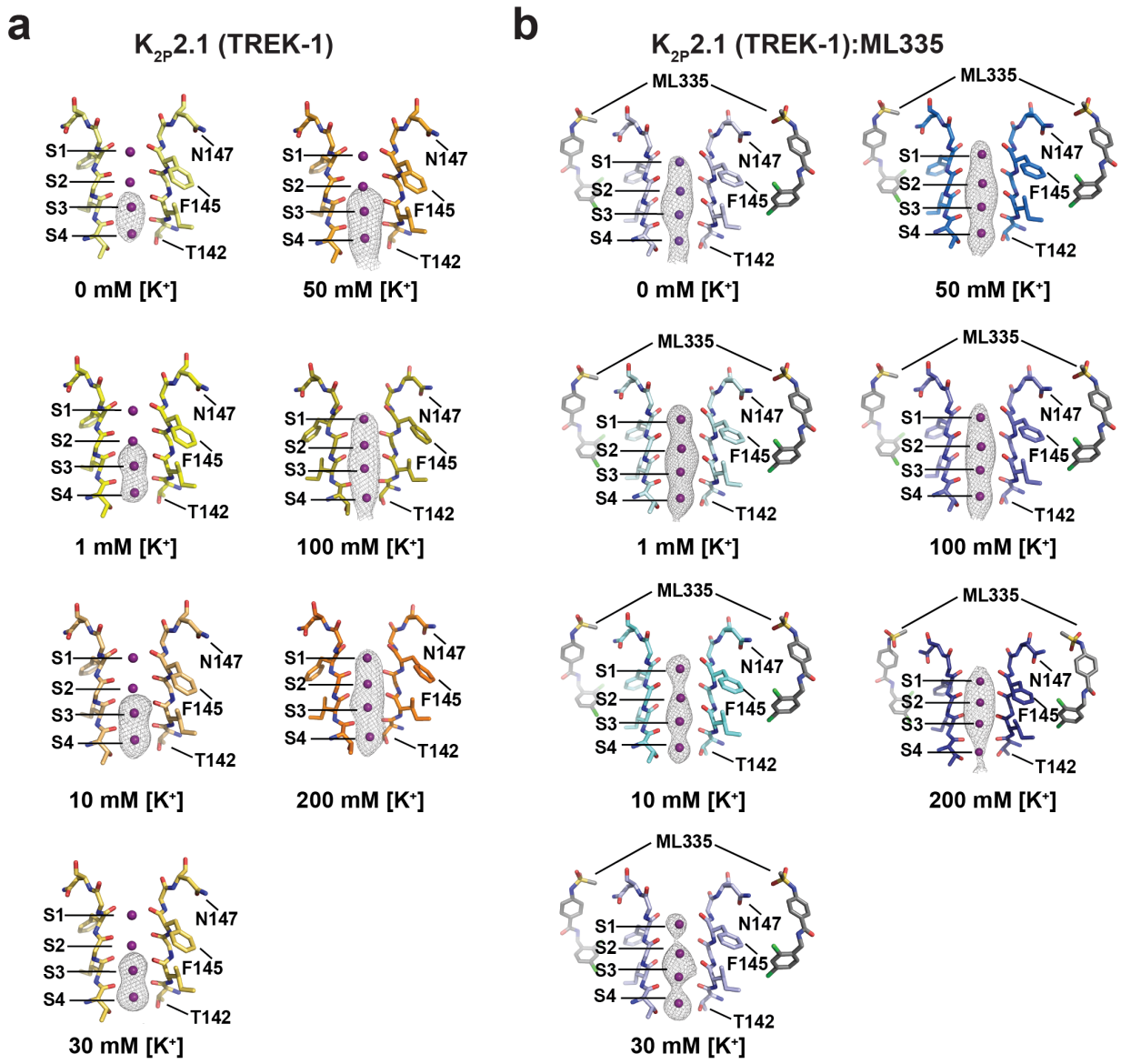

Fig. S4 Omit maps showing K_{2P}2.1 (TREK-1) selectivity filter ion occupancy as a function of [K+]. **a,b,** Polder omit maps(*28*) for structures of K_{2P}2.1 (TREK-1) determined in 0 mM [K+] (pale yellow) (5σ), 1 mM [K+] (yellow) (4σ), 10 mM [K+] (light orange) (5σ), 30 mM [K+] (yellow orange) (4σ), 50 mM [K+] (bright orange)(5σ), 100 mM [K+] (olive) (4σ), and 200 mM [K+] (orange)(4σ) (**a**) or K_{2P}2.1 (TREK-1):ML335 determined in 0 mM [K+] (blue white) (4σ), 1 mM [K+] (pale cyan) (4σ), 10 mM [K+] (aquamarine) (4σ), 30 mM [K+] (light blue) (4σ), 50 mM [K+] (marine) (4σ), 100 mM [K+] (slate) (4σ) and 200 mM [K+] (deep blue) (4σ) (**b**). Potassium ions are magenta spheres. Sites S1-S4 are labeled. ML335 is shown as sticks. SF1 in the 200 mM [K+] conformation is shown for all panels. Select residues are indicated.

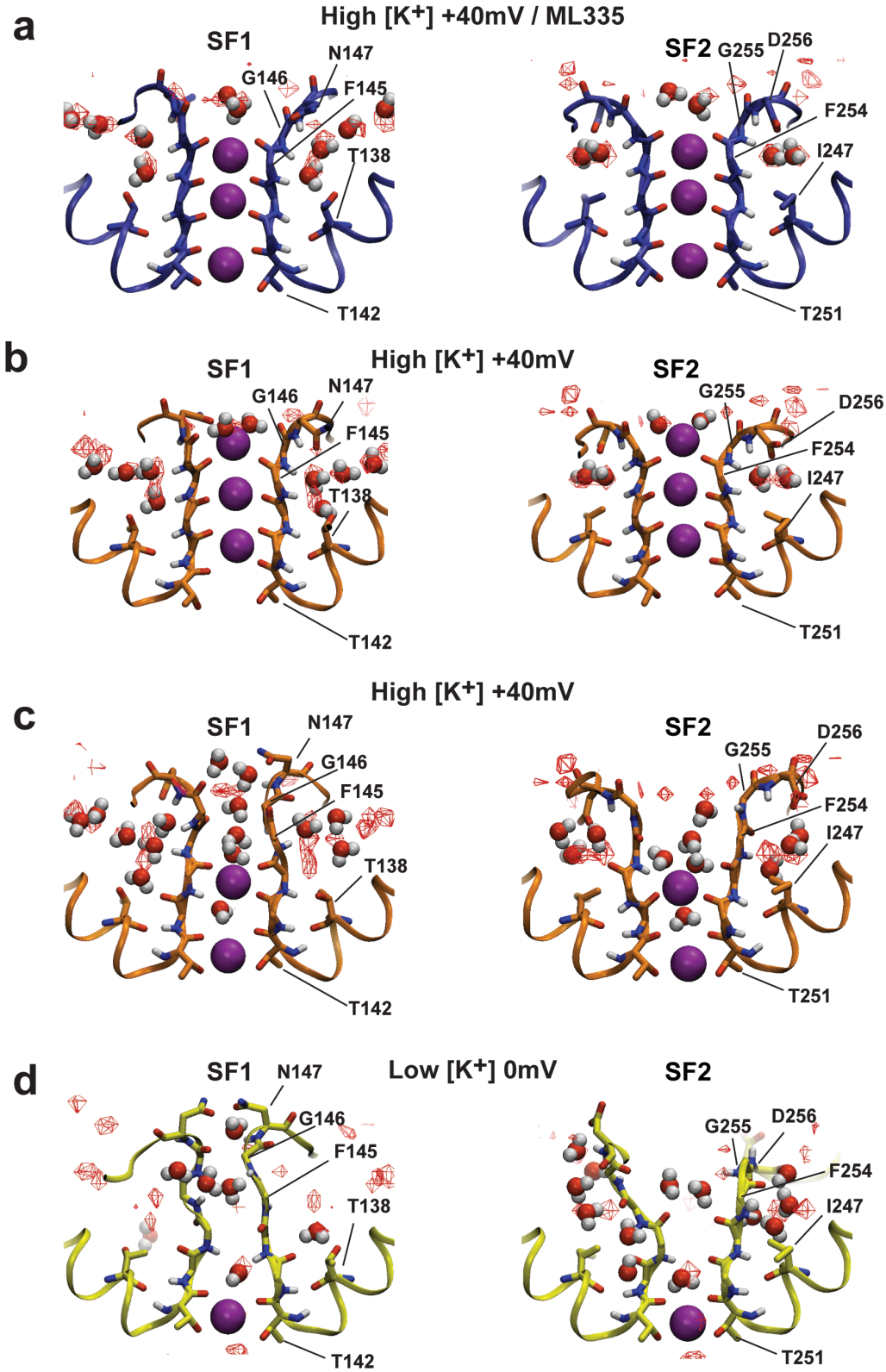

Fig. S5 Water interactions with the selectivity filter. a, Final frame of High [K+]/ +40 mV/ML335 simulation 4, showing SF1 (left) and SF2 (right). **b,** Final frame of High [K+]/+40 mV simulation 12. **c,** Final frame of High [K+]/+40 mV simulation 21. **d**, Final frame of Low [K+]/0 mV simulation 29. In all panels, water molecules interacting with the extracellular face of the selectivity filter are shown as spheres. Water oxygen

atom occupancy maps calculated from the simulation data are shown as red mesh and are contoured at the same level (density contains voxels with occupancy >7%) in all panels. Maps in **a** and **d** were calculated from all High [K^+]/+40 mV/ML335 and Low [K^+]/0 mV simulation trajectories, respectively. Map in **b** and **c** was calculated from all High [K^+]/+40 mV simulation trajectories. **c** and **d** show examples where filters have become disordered.

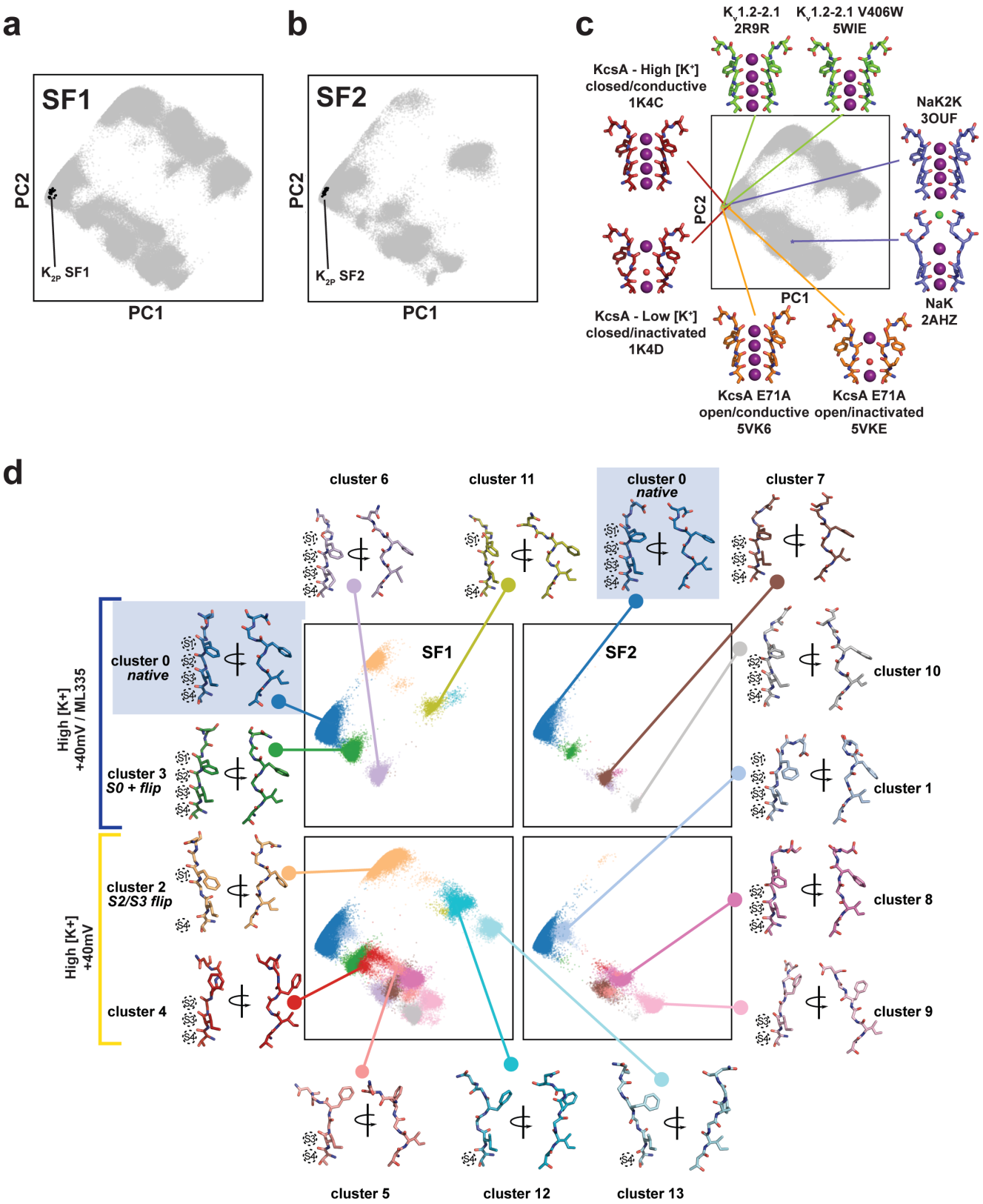

Fig. S6 K_{2P}2.1 (TREK-1) principal component analysis (PCA). a,b, PCA projection of selectivity filter conformations for SF1 (**a**) and SF2 (**b**). Grey points indicate K_{2P}2.1 (TREK-1) conformations from all simulations in this work; black points represent projections of SF1 and SF2 conformations obtained from

the Fig. S1b K_{2P} crystal structures. **c**, Representative non-K_{2P} selectivity filter conformations and their projections into PCA space. Grey points indicate K_{2P}2.1 (TREK-1) conformations from all simulations (SF1 and SF2). Lines and colored points show the PCA projected location of SF conformations from the indicated tetrameric potassium channel crystal structures: KcsA closed/conductive (1K4C) and closed/inactivated (1K4D)(*14*) (firebrick); Kv1.2-2.1 chimera (2R9R)(*33*) and V406W mutant (5WIE)(*17*) (chartreuse); NaK (2AHZ)(*36*) and K^+ selective mutant NaK2K (3OUF)(*27*) (slate); and KcsA E71A open/conductive (5VK6) and open/inactivated (5VKE)(*15*) (orange). **d**, Hierarchical clustering of SF conformations from all High [K^+] simulations. Clustering was performed on PC1-3, for clarity only PC1 and PC2 are shown. Points representing selectivity filter conformations in PCA space are colored according to their membership in one of 14 identified clusters. A single representative conformation is shown for each cluster, with the exception of the native state (cluster 0) for which representative conformations from both SF1 and SF2 are shown. For each representative conformation intact ion binding sites are indicated with dotted circles.

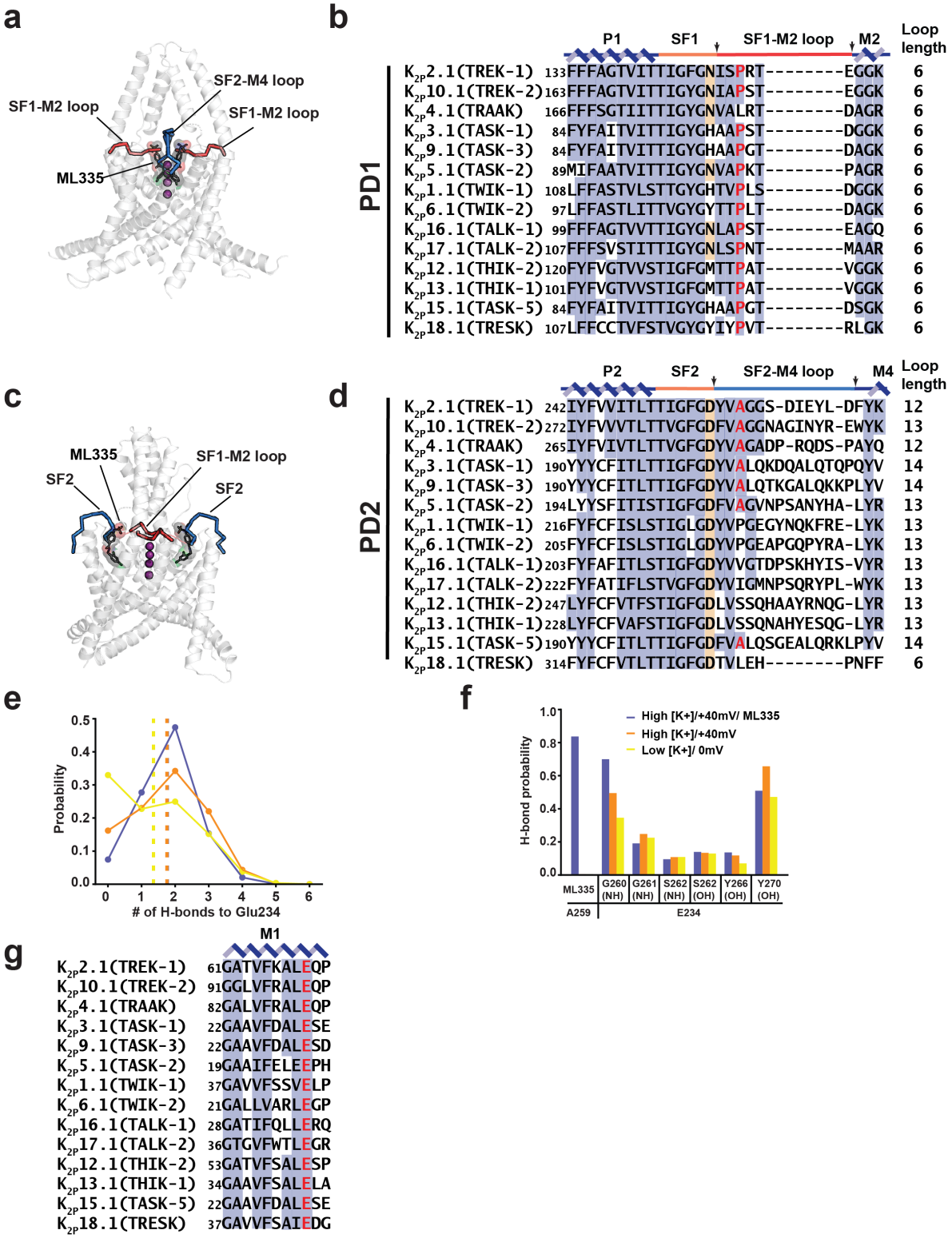

Fig. S7 K_{2P} channel pore domain comparisons. a, K_{2P}2.1 (TREK-1):ML335 complex (white) with a view showing the SF1-M2 loop. SF1-M2 loop (red) and SF2-M4 loop (blue) are indicted. ML335 (black) is shown in sticks with a transparent surface. **b,** Sequence alignment of PD1 for the indicated channels. P1 and M2 helices (blue), SF1 (orange), and SF1-M2 loop (red) are indicated. Terminal residue of the selectivity filter is highlighted. Arrows denote the boundaries of the SF1-M2 loop. **c,** K_{2P}2.1 (TREK-1):ML335 complex

(white) with a view showing the SF2-M4 loop. SF1-M2 loop (red) and SF2-M4 loop (blue) are indicted. ML335 (black) is shown in sticks with a transparent surface. **d,** Sequence alignment of PD2 for the indicated channels. Conserved residues are shaded in slate. Dashed red and blue boxes indicate the SF1-M2 (**c**) and SF2-M4 loops (**d**). Conserved selectivity filter N/D is shaded orange. Pro150, Ala259, and equivalents are shaded red. **e,** Per-frame probability of finding a particular number of hydrogen bonds to the Glu234 sidechain carboxylate in all K_{2P}2.1 (TREK-1) simulations. Dotted lines indicate the overall average number of hydrogen bonds calculated for each simulation condition. **f,** Per-frame probability of a hydrogen bond between the indicated groups in all K_{2P}2.1 (TREK-1) simulations. **g,** Sequence alignment of M1 for the indicated channels. Conserved glutamate is highlighted red.

Sequences (**b**,**d**, and **g**) are from human K_{2P} channels: K_{2P}2.1 (TREK-1) AAD47569.1, K_{2P}10.1 (TREK-2) NP_612190.1, K_{2P}4.1 (TRAAK) AAI10328.1, K_{2P}3.1 (TASK-1) NP_002237.1, K_{2P}9.1 (TASK-3) NP_001269463.1, K_{2P}5.1 (TASK-2) NP_003731.1, K_{2P}1.1(TWIK-1) NP_002236.1, K_{2P}6.1 (TWIK-2) NP_004814.1, K_{2P}16.1 (TALK-1) NP_115491.1, K_{2P}17.1 (TALK-2) AAK28551.1, K_{2P}12.1 (THIK-2) NP_071338.1, K_{2P}13.1 (THIK-1) NP_071337.2, K_{2P}15.1 (TASK-5) EAW75900.1, K_{2P}18.1 (TRESK) NP_862823.1. SF1 and SF2 sequence and numbers for K_{2P}2.1 (TREK-1)$_{cryst}$ (PDB:6CQ6)(*20*) are identical to that of K_{2P}2.1 (TREK-1) AAD47569.1.

Fig. S8 Lolicato *et al.*

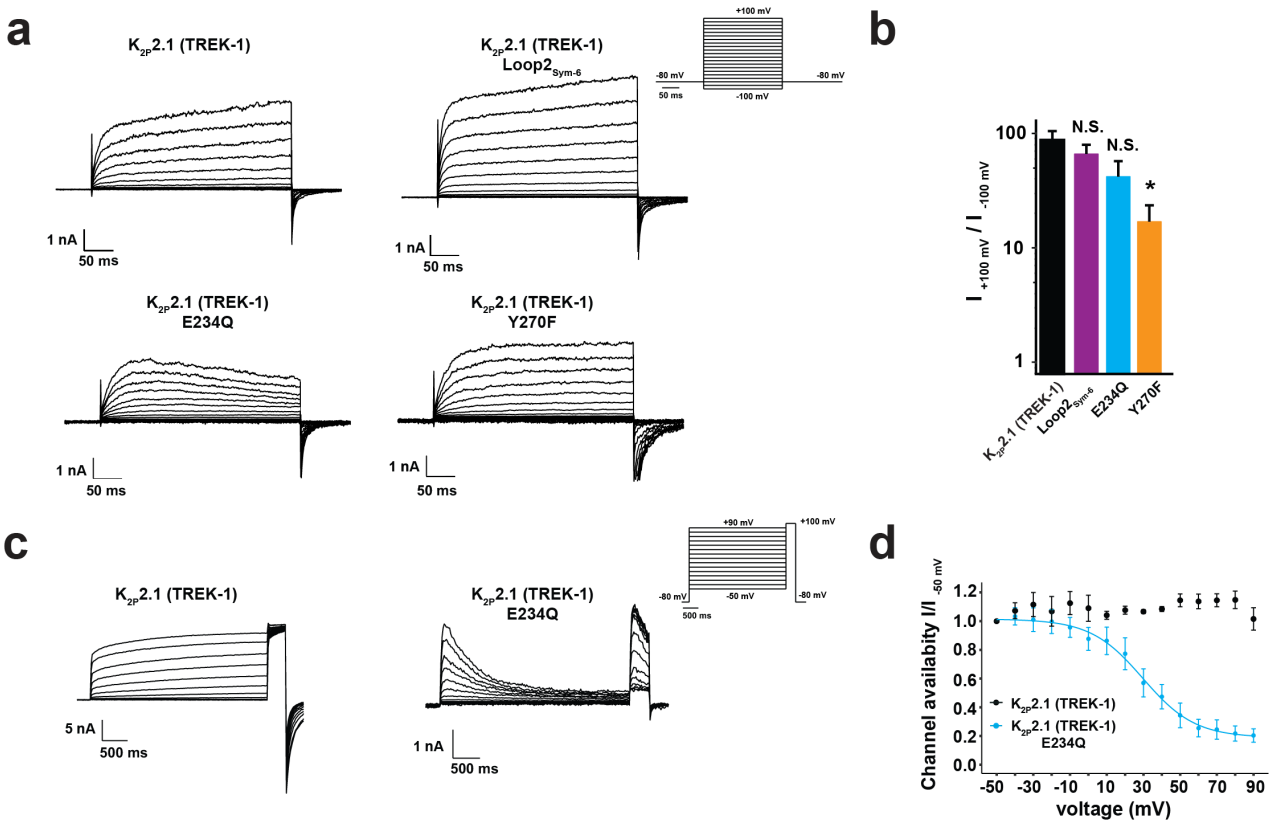

Fig. S8 K_{2P} patch clamp recordings. a, Exemplar current traces from inside-out membrane patches of HEK293 cells expressing $K_{2P}2.1$ (TREK-1), $K_{2P}2.1$ (TREK-1) E234Q, $K_{2P}2.1$ (TREK-1) Y270F, or $K_{2P}2.1$ (TREK1) $Loop2_{Sym6}$, in 150 mM $K^+_{[ext]}$/150 mM $Rb^+_{[int]}$. Inset shows voltage protocol. **b**, Rectification coefficients ($I_{+100mV}/-I_{-100mV}$) calculated from currents recorded on $n \geq 5$ individual patches. * $p < 0.05$ compared to $K_{2P}2.1$ (TREK-1). N.S, not statistically different. **c,** Exemplar current traces from inside-out membrane patches of HEK293 cells expressing $K_{2P}2.1$ (TREK-1) or $K_{2P}2.1$ (TREK-1) E234Q in response to an inactivation protocol (inset). **d,** Channel availability curves determined by plotting the normalized peak currents (I/I_{-50mV}) measured at +100 mV as a function of pre-pulse voltages ($n \geq 4$). For panels **b,** and **d,** data represent mean ± s.e.m.

Fig. S9 Lolicato *et al.*

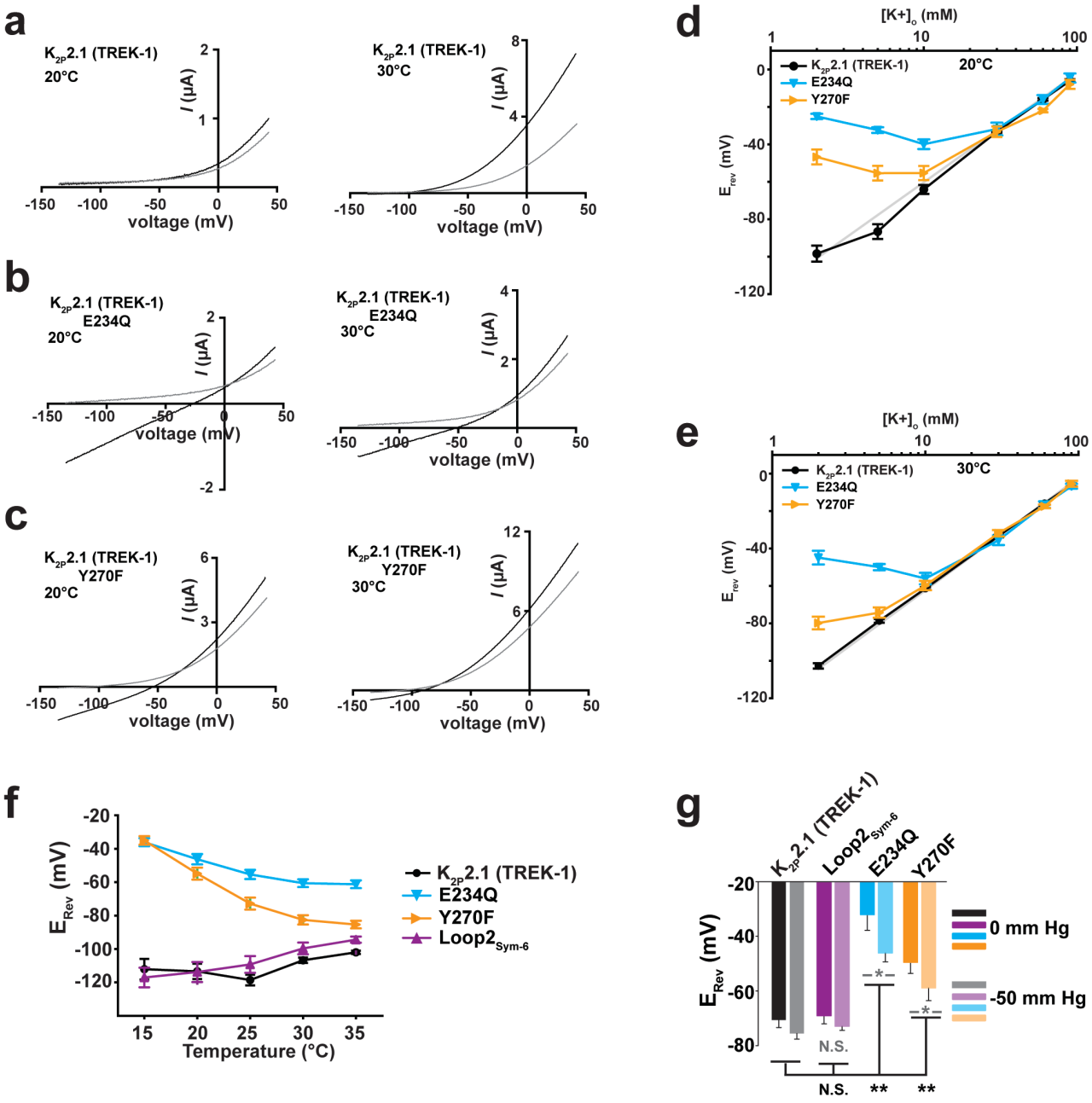

Fig. S9 Activation alters K_{2P}2.1 (TREK-1) mutant ion selectivity. a-c, Exemplar two-electrode voltage clamp (TEVC) recordings of K_{2P}2.1 (TREK-1) (**a**), K_{2P}2.1 (TREK-1) E234Q (**b**), and K_{2P}2.1 (TREK-1) Y270F (**c**) at 20°C (left) and 30°C (right) in solutions of 96 mM Na^+/2 mM K^+ (black) or 96 mM *N*-methyl-D-glucamine/2 mM K^+ (grey). **d,** and **e,** Potassium selectivity recorded in *Xenopus* oocytes in K^+/Na^+ solutions (98.0 mM total) at pH_o = 7.4 at **d**, 20°C and **e**, 30°C (n=6). Data are background subtracted using uninjected oocytes. Grey line represents Nernst equation $E_{rev} = RT/F \times \log([K^+]_o/[K^+]_i)$, where R and F have their usual thermodynamic meanings, z is equal to 1, and T = 20°C or 30°C, assuming $[K^+]_i$ = 108.6 mM ((*110*)). **f,** E_{rev} as a function of temperature for the indicated channels from TEVC experiments in *Xenopus* oocytes. **g,** E_{rev} at 0 and -50 mmHg measured from inside-out membrane patches of HEK293 cells expressing the indicated channels. * $p < 0.05$ compared to K_{2P}2.1 (TREK-1) at the same pressure.

N.S, not statistically different. ($n \geq 4$). Grey indicates statistical significance between the 0 mM and -50 mM Hg measurements. For panels (**d**)-(**g**), data represent mean ± s.e.m.

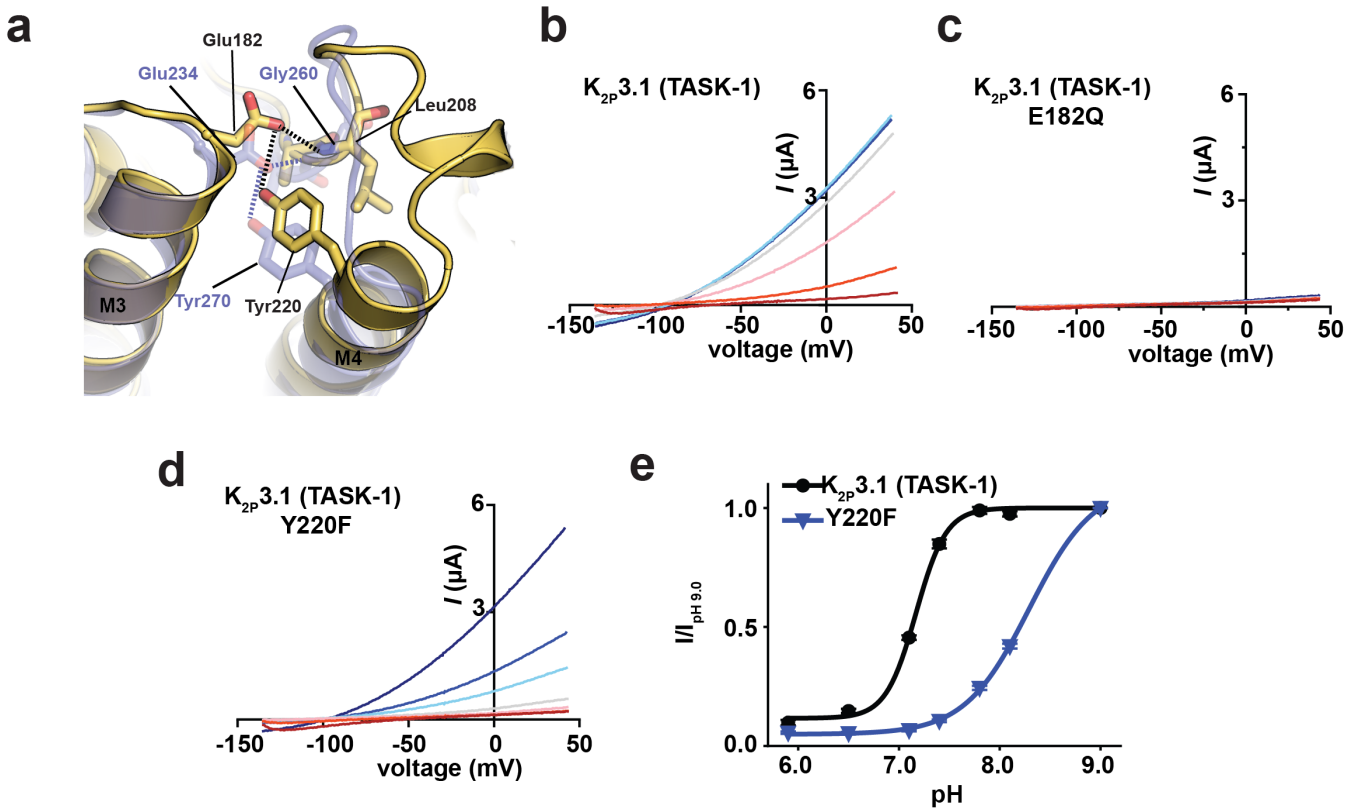

Fig. S10 M3 glutamate network destabilization facilitates K_{2P}3.1(TASK-1) C-type gate closure. **a,** Comparison of the SF2-M4 loop and surrounding elements K_{2P}3.1 (TASK-1) (PDB: 6RV2)(*43*) (yellow) and K_{2P}2.1 (TREK-1) (PBD:6CQ8)(*20*) (transparent purple). Key network residues are shown as sticks and are labeled. Dashed lines show hydrogen bonds. **b-d**, Exemplar two-electrode voltage clamp (TEVC) recordings of **b,** K_{2P}3.1 (TASK-1), **c**, K_{2P}3.1 (TASK-1) E182Q, and **d**, K_{2P}3.1 (TASK1) Y220F at pH_{ext}: 9.0 (dark blue), 8.1 (blue), 7.8 (light blue), 7.4 (grey), 7.1 (pink), 6.5 (red), 5.9 (maroon). **e**, pH activation curves for K_{2P}3.1 (TASK-1) (black) and K_{2P}3.1 (TASK1) Y220F (blue), showing the fraction of the current at 0 mV at each pH relative to the current at pH 9.0 (n≥10). Data in '**e**' represent the mean ± s.e.m. (n≥10).

Supplementary Movie 1 High [K^+]/+40 mV simulation trajectory. Pore helix 1 and SF1-M2 loop are shown in cartoon representation, SF1 is shown as sticks, and potassium ions are spheres of varying colors. Movie represents the first 1920 ns of simulation 1.

Supplementary Movie 2 Low [K^+]/0 mV simulation trajectory. Pore helix 2 and SF2-M4 loop are shown in cartoon representation, SF2 is shown as sticks, M4 is shown as transparent cartoon, and the potassium ion is shown as a magenta sphere. Residues involved in the Glu234 network are shown as green sticks. Movie represents the first 1920 ns of simulation 29.

Supplementary Movie 3 Morph between the SF1 active and inactive conformations. 0 mM [K^+]:ML335 structures and 1 mM [K^+] structures represent the active and inactive conformations, respectively. Selectivity filter is yellow orange. Asn147 and Thr142 are shown as sticks. Potassium ions are magenta spheres.

Supplementary Movie 4 Morph between the SF2 active and inactive conformations. 0 mM [K^+]:ML335 structures and 1 mM [K^+] structures represent the active and inactive conformations, respectively. Selectivity filter is yellow orange. Asp256 and Thr251 are shown as sticks. Potassium ions are magenta spheres.

Table S1 Data collection and refinement statistics $K_{2P}2.1$ (TREK-1) and $K_{2P}2.1$ (TREK-1):ML335 complex structures

Condition	0mM [K+]	1mM [K+]	10mM [K+	30mM [K+]	50mM [K+]	100mM [K+]	200mM [K+]
PDB code	**6W7B**	**6W7C**	**6W7D**	**6W7E**	**6W82**	**6W83**	**6W84**
Data collection							
Space group	$P2_12_12_1$	$P2_12_12_1$	$P2_12_12_1$	$P2_12_12_1$	$P2_12_12_1$	$P2_12_12_1$	$P2_12_12_1$
Cell dimensions							
a, *b*, *c* (Å)	66.91, 122.60, 125.58	66.501, 123.014, 125.848	67.306 122.652 126.127	67.368 122.534 126.552	67.487, 122.067, 126.861	70.222, 121.164, 129.426	70.627, 121.287, 130.034
α, β, γ (°)	90, 90, 90	90, 90, 90	90, 90, 90	90, 90, 90	90, 90, 90	90, 90, 90	90, 90, 90
Resolution (Å)	45.8 - 3.9 (4.0 - 3.9)	44.0 - 3.4 (3.5 - 3.4)	46.0 - 3.5 (3.6 - 3.5)	46.1 - 3.3 (3.4 - 3.3)	46.2 - 3.6 (3.7 - 3.6)	47.6 - 3.9 (4.0 - 3.9)	47.8 - 3.7 (3.8 - 3.7)
$R_{merge,}$	0.196 (7.9)	0.096 (5.14)	0.078 (5.21)	0.051 (5.61)	0.060 (3.01)	0.204 (11.0)	0.141 (9.29)
$I/\sigma(I)$	2.95 (0.34)	9.01 (0.28)	8.20 (0.31)	19.37 (0.44)	8.90 (0.46)	5.80 (0.17)	8.13 (0.22)
$CC_{1/2}$	0.995 (0.264)	0.998 (0.147)	0.998 (0.225)	0.999 (0.326)	0.999 (0.165)	0.997 (0.113)	0.999 (0.120)
Completeness (%)	99.3(99.3)	99.9(100)	99.12 (100)	99.30 (99.9)	99.1 (99.7)	99.9 (99.9)	99.9 (99.6)
Redundancy	4.9 (4.9)	6.5 (6.5)	6.6 (6.7)	11.7 (11.8)	3.6 (3.8)	11.8 (11.3)	13.2 (13.5)
Refinement							
Resolution (Å)	15.0 - 3.9	15.0 – 3.4	15.0 – 3.5	15.0 – 3.3	15.0 – 3.6	15.0 – 3.9	15.0 – 3.7
No. reflections	48795 (4680)	96014 (9500)	90434 (8933)	194227 (19500)	45124 (4759)	123755 (11519)	161238 (15874)
Unique reflections	9972 (955)	14774 (1463)	13692 (1326)	16544 (1647)	12522 (1239)	10520 (1019)	12209 (1174)
R_{work} / R_{free}	0.30/0.36	0.287/0.315	0.276/0.301	0.273/0.317	0.266/0.332	0.264/0.335	0.269/0.339
No. atoms	4168	4234	4263	4204	4295	4366	4353
Protein	4083	4111	4149	4073	4186	4283	4289
Ligand/ion	85	114	123	131	109	83	64
K^+	2	3	2	2	2	6	5
Cd^{++}	2	3	3	3	1	3	3
Lipid	81	108	118	126	106	74	56
ML335	0	0	0	0	0	0	0
B factors							
Protein	235.72	178.88	106.22	154.20	207.38	212.33	167.62
Ligand/ion	183.55	130.71	49.96	158.51	165.76	146.73	67.27
R.m.s. deviations							
Bond lengths (Å)	0.003	0.002	0.004	0.003	0.003	0.003	0.002
Bond angles (°)	0.76	0.62	0.79	0.71	0.65	0.72	0.59
Ramachandran							
Favored (%)	95.1	94.8	94.5	96.22	94.5	95.38	94.67
Allowed (%)	4.9	5.0	5.3	3.78	5.5	4.44	5.15
Outliers (%)	0.0	0.2	0.2	0.0	0.0	0.18	0.18

[a] Values in parentheses are for highest-resolution shell.
Each data set is from a single crystal.

Table S1 Data collection and refinement statistics $K_{2P}2.1$ (TREK-1) and $K_{2P}2.1$ (TREK-1):ML335 complex structures

Condition	ML335:0mM [K+]	ML335:1mM [K+]	ML335:10mM [K+]	ML335:30mM [K+]	ML335:50mM [K+]	ML335:100mM [K+]	ML335:200mM [K+]
PDB code	**6W8F**	**6W8C**	**6W8A**	**6W88**	**6W87**	**6W86**	**6W85**
Data collection							
Space group	$P2_12_12_1$	$P2_12_12_1$	$P2_12_12_1$	$P2_12_12_1$	$P2_12_12_1$	$P2_12_12_1$	$P2_12_12_1$
Cell dimensions							
a, *b*, *c* (Å)	66.671, 119.963, 128.941	67.129, 119.783, 128.872	66.867, 119.951, 129.245	67.006,119.996, 128.794	66.944, 119.48, 128.393	67.317, 120.133, 129.431	70.177, 120.65, 129.795
α, β, γ (°)	90, 90, 90	90, 90, 90	90, 90, 90	90, 90, 90	90, 90, 90	90, 90, 90	90, 90, 90
Resolution (Å)	44.6 - 3.4 (3.5 - 3.4)	46.5 - 2.6 (2.7 - 2.6)	46.5 - 3.0 (3.1 - 3.0)	43.3 - 3.2 (3.3 - 3.2)	44.6 - 3.2 (3.3 - 3.2)	43.5 - 3.3 (3.4 - 3.3)	47.6 - 3.8 (3.9 - 3.8)
$R_{merge,}$	0.117 (4.845)	0.1019 (4.052)	0.1307 (9.36)	0.1337 (4.951)	0.1028 (3.779)	0.1768 (6.905)	0.11 (8.314)
$I/\sigma(I)$	6.04 (0.27)	9.23 (0.40)	6.38 (0.28)	5.38 (0.29)	11.12 (0.53)	5.08 (0.34)	6.66 (0.17)
$CC_{1/2}$	0.995 (0.158)	0.997 (0.192)	0.997 (0.108)	0.996 (0.341)	0.999 (0.199)	0.998 (0.163)	1 (0.113)
Completeness (%)	94.1 (95.0)	98.8 (100)	97.11 (98.8)	95.9 (99.1)	99.81 (99.8)	98.7 (99.4)	99.9 (99.8)
Redundancy	3.9 (3.9)	6.7 (6.9)	5.8 (6.0)	4.7 (5.1)	7.2 (7.0)	6.5 (6.9)	5.9 (6.0)
Refinement							
Resolution (Å)	15.0 – 3.4	15.0 – 2.6	15.0 – 3.0	15.0 – 3.2	15.0 – 3.2	15.0 – 3.3	15.0 – 3.8
No. reflections	54265 (5332)	217375 (22304)	123425 (12506)	81728 (8687)	126742 (11910)	106948 (11156)	65640 (6466)
Unique reflections	13806 (1383)	32673 (3216)	21121 (2069)	17465 (1691)	17607 (1707)	16386 (1623)	11133 (1083)
R_{work} / R_{free}	0.257/0.288	0.243/0.287	0.25/0.271	0.266/0.33	0.24/0.314	0.248/0.295	0.244/0.317
No. atoms	4557	4741	4558	4573	4568	4516	4467
Protein	4349	4341	4349	4358	4343	4349	4350
Ligand/ion	208	399	209	215	225	167	117
K^+	4	6	5	5	5	5	5
Cd^{++}	4	3	4	4	4	3	2
Lipid	154	344	154	160	170	113	64
ML335	46	46	46	46	46	46	46
B factors							
Protein	160.79	118.49	66.39	90.12	141.11	146.49	232.41
Ligand/ion	140.87	134.81	51.59	74.87	125.60	127.03	185.26
R.m.s. deviations							
Bond lengths (Å)	0.002	0.014	0.003	0.006	0.010	0.011	0.011
Bond angles (°)	0.65	1.74	0.70	1.10	1.43	1.49	1.41
Ramachandran							
Favored (%)	95.1	92.71	95.81	93.64	93.07	91.62	93.26
Allowed (%)	4.5	6.38	3.83	6.00	6.02	7.29	5.83
Outliers (%)	0.4	0.91	0.36	0.36	0.91	1.09	0.91

[a] Values in parentheses are for highest-resolution shell.

Each data set is from a single crystal.

Table S2 Anomalous peak heights (in σ)

	1 mM [K^+]	200mM [K^+]	ML335:1mM [K^+]	ML335:200mM [K^+]
Filter site				
S1	2.25	6.24	5.47	6.09
S2	3.10	7.64	6.12	7.01
S3	6.24	8.30	6.40	8.23
S4	3.89	6.19	4.38	4.09
Resolution (Å)	5.5	5.7	5.0	5.5

Anomalous peak heights (in σ) from long-wavelength data above (λ = 3.35 Å) the potassium K-edge as calculated with ANODE(*86*) based on $K_{2P}2.1$ (TREK-1) (6CQ6)(*20*).

Table S3 Molecular dynamics simulations

ID	PDBID	n atoms	Engine	[K^+] (mM)	ML335	Potential (mV)	Length (ns)	n permeations
1	6W8C	205060	Anton2	180	yes	+40	2880	26
2	6W8C	205060	Anton2	180	yes	+40	2880	23
3	6W8C	205060	Anton2	180	yes	+40	2880	9
4	6W8C	205060	Anton2	180	yes	+40	3840	30
5	6W8C	205060	Anton2	180	yes	+40	2880	35
6	6W8C	205228	Anton2	180	yes	+40	3840	26
7	6W8C	205228	Anton2	180	yes	+40	2880	20
8	6W8C	205228	Anton2	180	yes	+40	2880	2
9	6W8C	205228	Anton2	180	yes	+40	2880	29
10	6W8C	205228	Anton2	180	yes	+40	3840	53
11	5VK5	205159	Anton2	180	no	+40	4800	3
12	5VK5	205159	Anton2	180	no	+40	4800	36
13	6CQ6	205175	Anton2	180	no	+40	1920	3
14	6CQ6	205175	Anton2	180	no	+40	1920	2
15	6CQ6	205175	Anton2	180	no	+40	1920	2
16	6CQ6	205175	Anton2	180	no	+40	1920	-1
17	6CQ6	205175	Anton2	180	no	+40	2880	19
18	6CQ6	205325	Anton2	180	no	+40	3840	20
19	6CQ6	205325	Anton2	180	no	+40	2880	18
20	6CQ6	205325	Anton2	180	no	+40	2880	6
21	6CQ6	205325	Anton2	180	no	+40	2880	2
22	6CQ6	205325	Anton2	180	no	+40	3840	34
23	6CQ6	204174	gromacs	5	no	0	1400	-
24	6CQ6	204168	gromacs	5	no	0	2400	-
25	6CQ6	204168	gromacs	5	no	0	2000	-
26	6CQ6	204006	gromacs	5	no	0	2000	-
27	6CQ6	204006	gromacs	5	no	0	2000	-
28	6CQ6	204174	Anton2	5	no	0	3600	-
29	6CQ6	204441	Anton2	5	no	0	3600	-
30	6CQ6	204006	Anton2	5	no	0	3600	-

REFERENCES AND NOTES

1. P. Enyedi, G. Czirjak, Molecular background of leak K^+ currents: Two-pore domain potassium channels. *Physiol. Rev.* **90**, 559–605 (2010).

2. S. Feliciangeli, F. C. Chatelain, D. Bichet, F. Lesage, The family of K2P channels: Salient structural and functional properties. *J. Physiol.* **593** (Pt. 12), 2587–2603 (2015).

3. S. N. Bagriantsev, K. A. Clark, D. L. Minor, Jr., Metabolic and thermal stimuli control K(2P)2.1 (TREK-1) through modular sensory and gating domains. *EMBO J.* **31**, 3297–3308 (2012).

4. S. N. Bagriantsev, R. Peyronnet, K. A. Clark, E. Honore, D. L. Minor Jr., Multiple modalities converge on a common gate to control K2P channel function. *EMBO J.* **30**, 3594–3606 (2011).

5. M. Schewe, E. Nematian-Ardestani, H. Sun, M. Musinszki, S. Cordeiro, G. Bucci, B. L. de Groot, S. J. Tucker, M. Rapedius, T. Baukrowitz, A non-canonical voltage-sensing mechanism controls gating in K2P K^+ channels. *Cell* **164**, 937–949 (2016).

6. P. L. Piechotta, M. Rapedius, P. J. Stansfeld, M. K. Bollepalli, G. Erhlich, I. Andres-Enguix, H. Fritzenschaft, N. Decher, M. S. P. Sansom, S. J. Tucker, T. Baukrowitz, The pore structure and gating mechanism of K2P channels. *EMBO J.* **30**, 3607–3619 (2011).

7. J. Lopez-Barneo, T. Hoshi, S. H. Heinemann, R. W. Aldrich, Effects of external cations and mutations in the pore region on C-type inactivation of Shaker potassium channels. *Receptors Channels* **1**, 61–71 (1993).

8. T. Baukrowitz, G. Yellen, Modulation of K^+ current by frequency and external $[K^+]$: A tale of two inactivation mechanisms. *Neuron* **15**, 951–960 (1995).

9. L. A. Pardo, S. H. Heinemann, H. Terlau, U. Ludewig, C. Lorra, O. Pongs, W. Stuhmer, Extracellular K^+ specifically modulates a rat brain K+ channel. *Proc. Natl. Acad. Sci. U.S.A.* **89**, 2466–2470 (1992).

10. A. Cohen, Y. Ben-Abu, S. Hen, N. Zilberberg, A novel mechanism for human $K_{2P}2.1$ channel gating. Facilitation of C-type gating by protonation of extracellular histidine residues. *J. Biol. Chem.* **283**, 19448–19455 (2008).

11. J. F. Cordero-Morales, L. G. Cuello, Y. Zhao, V. Jogini, D. M. Cortes, B. Roux, E. Perozo, Molecular determinants of gating at the potassium-channel selectivity filter. *Nat. Struct. Mol. Biol.* **13**, 311–318 (2006).

12. T. Hoshi, C. M. Armstrong, C-type inactivation of voltage-gated K^+ channels: Pore constriction or dilation? *J. Gen. Physiol.* **141**, 151–160 (2013).

13. Y. Zhou, R. MacKinnon, The occupancy of ions in the K^+ selectivity filter: Charge balance and coupling of ion binding to a protein conformational change underlie high conduction rates. *J. Mol. Biol.* **333**, 965–975 (2003).

14. Y. Zhou, J. H. Morais-Cabral, A. Kaufman, R. MacKinnon, Chemistry of ion coordination and hydration revealed by a K^+ channel-Fab complex at 2.0 Å resolution. *Nature* **414**, 43–48 (2001).

15. L. G. Cuello, D. M. Cortes, E. Perozo, The gating cycle of a K^+ channel at atomic resolution. *eLife* **6**, e28032 (2017).

16. L. G. Cuello, V. Jogini, D. M. Cortes, E. Perozo, Structural mechanism of C-type inactivation in K^+ channels. *Nature* **466**, 203–208 (2010).

17. V. Pau, Y. Zhou, Y. Ramu, Y. Xu, Z. Lu, Crystal structure of an inactivated mutant mammalian voltage-gated K^+ channel. *Nat. Struct. Mol. Biol.* **24**, 857–865 (2017).

18. W. Wang, R. MacKinnon, Cryo-EM structure of the open human ether-à-go-go-related K^+ Channel hERG. *Cell* **169**, 422–430.e10 (2017).

19. D. Matthies, C. Bae, G. E. S. Toombes, T. Fox, A. Bartesaghi, S. Subramaniam, K. J. Swartz, Single-particle cryo-EM structure of a voltage-activated potassium channel in lipid nanodiscs. *eLife* **7**, e37558 (2018).

20. M. Lolicato, C. Arrigoni, T. Mori, Y. Sekioka, C. Bryant, K. A. Clark, D. L. Minor Jr, $K_{2P}2.1$ (TREK-1)–activator complexes reveal a cryptic selectivity filter binding site. *Nature* **547**, 364–368 (2017).

21. Y. Y. Dong, A. C. W. Pike, A. Mackenzie, C. McClenaghan, P. Aryal, L. Dong, A. Quigley, M. Grieben, S. Goubin, S. Mukhopadhyay, G. F. Ruda, M. V. Clausen, L. Cao, P. E. Brennan, N. A. Burgess-Brown, M. S. P. Sansom, S. J. Tucker, E. P. Carpenter, K2P channel gating mechanisms revealed by structures of TREK-2 and a complex with Prozac. *Science* **347**, 1256–1259 (2015).

22. S. G. Brohawn, J. del Marmol, R. MacKinnon, Crystal structure of the human K2P TRAAK, a lipid- and mechano-sensitive K^+ ion channel. *Science* **335**, 436–441 (2012).

23. S. G. Brohawn, E. B. Campbell, R. MacKinnon, Domain-swapped chain connectivity and gated membrane access in a Fab-mediated crystal of the human TRAAK K^+ channel. *Proc. Natl. Acad. Sci. U.S.A.* **110**, 2129–2134 (2013).

24. S. G. Brohawn, E. B. Campbell, R. MacKinnon, Physical mechanism for gating and mechanosensitivity of the human TRAAK K^+ channel. *Nature* **516**, 126–130 (2014).

25. M. Lolicato, P. M. Riegelhaupt, C. Arrigoni, K. A. Clark, D. L. Minor Jr., Transmembrane helix straightening and buckling underlies activation of mechanosensitive and thermosensitive K(2P) channels. *Neuron* **84**, 1198–1212 (2014).

26. A. N. Miller, S. B. Long, Crystal structure of the human two-pore domain potassium channel K2P1. *Science* **335**, 432–436 (2012).

27. M. G. Derebe, D. B. Sauer, W. Zeng, A. Alam, N. Shi, Y. Jiang, Tuning the ion selectivity of tetrameric cation channels by changing the number of ion binding sites. *Proc. Natl. Acad. Sci. U.S.A.* **108**, 598–602 (2011).

28. D. Liebschner, P. V. Afonine, N. W. Moriarty, B. K. Poon, O. V. Sobolev, T. C. Terwilliger, P. D. Adams, Polder maps: Improving OMIT maps by excluding bulk solvent. *Acta Crystallogr. D Struct. Biol.* **73**, 148–157 (2017).

29. P. S. Langan, V. G. Vandavasi, K. L. Weiss, P. V. Afonine, K. el Omari, R. Duman, A. Wagner, L. Coates, Anomalous x-ray diffraction studies of ion transport in K^+ channels. *Nat. Commun.* **9**, 4540 (2018).

30. A. Wagner, R. Duman, K. Henderson, V. Mykhaylyk, In-vacuum long-wavelength macromolecular crystallography. *Acta Crystallogr. D Struct. Biol.* **72**, 430–439 (2016).

31. J. Ostmeyer, S. Chakrapani, A. C. Pan, E. Perozo, B. Roux, Recovery from slow inactivation in K^+ channels is controlled by water molecules. *Nature* **501**, 121–124 (2013).

32. A. Altis, P. H. Nguyen, R. Hegger, G. Stock, Dihedral angle principal component analysis of molecular dynamics simulations. *J. Chem. Phys.* **126**, 244111 (2007).

33. S. B. Long, X. Tao, E. B. Campbell, R. MacKinnon, Atomic structure of a voltage-dependent K^+ channel in a lipid membrane-like environment. *Nature* **450**, 376–382 (2007).

34. J. T. Brennecke, B. L. de Groot, Mechanism of mechanosensitive gating of the TREK-2 potassium channel. *Biophys. J.* **114**, 1336–1343 (2018).

35. M. P. Harrigan, K. A. McKiernan, V. Shanmugasundaram, R. A. Denny, V. S. Pande, Markov modeling reveals novel intracellular modulation of the human TREK-2 selectivity filter. *Sci. Rep.* **7**, 632 (2017).

36. N. Shi, S. Ye, A. Alam, L. Chen, Y. Jiang, Atomic structure of a Na^+- and K^+-conducting channel. *Nature* **440**, 570–574 (2006).

37. L. Pope, C. Arrigoni, H. Lou, C. Bryant, A. Gallardo-Godoy, A. R. Renslo, D. L. Minor Jr., Protein and chemical determinants of BL-1249 action and selectivity for K_{2P} channels. *ACS Chem. Nerosci.* **9**, 3153–3165 (2018).

38. M. Schewe, H. Sun, Ü. Mert, A. Mackenzie, A. C. W. Pike, F. Schulz, C. Constantin, K. S. Vowinkel, L. J. Conrad, A. K. Kiper, W. Gonzalez, M. Musinszki, M. Tegtmeier, D. C. Pryde, H. Belabed, M. Nazare, B. L. de Groot, N. Decher, B. Fakler, E. P. Carpenter, S. J. Tucker, T.

Baukrowitz, A pharmacological master key mechanism that unlocks the selectivity filter gate in K^+ channels. *Science* **363**, 875–880 (2019).

39. N. Zilberberg, N. Ilan, S. A. N. Goldstein, KCNKØ. *Neuron* **32**, 635–648 (2001).

40. H. P. Larsson, F. Elinder, A conserved glutamate is important for slow inactivation in K^+ channels. *Neuron* **27**, 573–583 (2000).

41. P. Ortega-Sáenz, R. Pardal, A. Castellano, J. López-Barneo, Collapse of conductance is prevented by a glutamate residue conserved in voltage-dependent K^+ channels. *J. Gen. Physiol.* **116**, 181–190 (2000).

42. G. Sandoz, D. Douguet, F. Chatelain, M. Lazdunski, F. Lesage, Extracellular acidification exerts opposite actions on TREK1 and TREK2 potassium channels via a single conserved histidine residue. *Proc. Natl. Acad. Sci. U.S.A.* **106**, 14628–14633 (2009).

43. K. E. J. Rödström, A. K. Kiper, W. Zhang, S. Rinné, A. C. W. Pike, M. Goldstein, L. J. Conrad, M. Delbeck, M. G. Hahn, H. Meier, M. Platzk, A. Quigley, D. Speedman, L. Shrestha, S. M. M. Mukhopadhyay, N. A. Burgess-Brown, S. J. Tucker, T. Müller, N. Decher, E. P. Carpenter, A lower X-gate in TASK channels traps inhibitors within the vestibule. *Nature* **582**, 443–447 (2020).

44. S. A. Pless, J. D. Galpin, A. P. Niciforovic, H. T. Kurata, C. A. Ahern, Hydrogen bonds as molecular timers for slow inactivation in voltage-gated potassium channels. *eLife* **2**, e01289 (2013).

45. J. P. Lees-Miller, Y. Duan, G. Q. Teng, K. Thorstad, H. J. Duff, Novel gain-of-function mechanism in K^+ channel-related long-QT syndrome: Altered gating and selectivity in the HERG1 N629D mutant. *Circ. Res.* **86**, 507–513 (2000).

46. W. E. Miranda, K. R. DeMarco, J. Guo, H. J. Duff, I. Vorobyov, C. E. Clancy, S. Y. Noskov, Selectivity filter modalities and rapid inactivation of the hERG1 channel. *Proc. Natl. Acad. Sci. U.S.A.* **117**, 2795–2804 (2020).

47. D. Bockenhauer, N. Zilberberg, S. A. N. Goldstein, KCNK2: Reversible conversion of a hippocampal potassium leak into a voltage-dependent channel. *Nat. Neurosci.* **4**, 486–491 (2001).

48. M. V. Clausen, V. Jarerattanachat, E. P. Carpenter, M. S. P. Sansom, S. J. Tucker, Asymmetric mechanosensitivity in a eukaryotic ion channel. *Proc. Natl. Acad. Sci. U.S.A.* **114**, E8343–E8351 (2017).

49. M. Lengyel, G. Czirják, P. Enyedi, Formation of functional heterodimers by TREK-1 and TREK-2 two-pore domain potassium channel subunits. *J. Biol. Chem.* **291**, 13649–13661 (2016).

50. J. Levitz, P. Royal, Y. Comoglio, B. Wdziekonski, S. Schaub, D. M. Clemens, E. Y. Isacoff, G. Sandoz, Heterodimerization within the TREK channel subfamily produces a diverse family of highly regulated potassium channels. *Proc. Natl. Acad. Sci. U.S.A.* **113**, 4194–4199 (2016).

51. S. Blin, I. Ben Soussia, E.-J. Kim, F. Brau, D. Kang, F. Lesage, D. Bichet, Mixing and matching TREK/TRAAK subunits generate heterodimeric K_{2P} channels with unique properties. *Proc. Natl. Acad. Sci. U.S.A.* **113**, 4200–4205 (2016).

52. P. Royal, A. Andres-Bilbe, P. Á. Prado, C. Verkest, B. Wdziekonski, S. Schaub, A. Baron, F. Lesage, X. Gasull, J. Levitz, G. Sandoz, Migraine-associated TRESK mutations increase neuronal excitability through alternative translation initiation and inhibition of TREK. *Neuron* **101**, 232–245.e6 (2019).

53. S. Blin, F. C. Chatelain, S. Feliciangeli, D. Kang, F. Lesage, D. Bichet, Tandem pore domain halothane-inhibited K^+ channel subunits THIK1 and THIK2 assemble and form active channels. *J. Biol. Chem.* **289**, 28202–28212 (2014).

54. V. Renigunta, X. Zou, S. Kling, G. Schlichthörl, J. Daut, Breaking the silence: Functional expression of the two-pore-domain potassium channel THIK-2. *Pflugers Arch.* **466**, 1735–1745 (2014).

55. A. P. Berg, E. M. Talley, J. P. Manger, D. A. Bayliss, Motoneurons express heteromeric TWIK-related acid-sensitive K^+ (TASK) channels containing TASK-1 (KCNK3) and TASK-3 (KCNK9) subunits. *J. Neurosci.* **24**, 6693–6702 (2004).

56. A. Mathie, E. L. Veale, K. P. Cunningham, R. G. Holden, P. D. Wright, Two-pore domain potassium channels as drug targets: Anesthesia and beyond. *Annu. Rev. Pharmacol. Toxicol.* 10.1146/annurev-pharmtox-030920-111536 (2020).

57. K. H. Yuill, P. J. Stansfeld, I. Ashmole, M. J. Sutcliffe, P. R. Stanfield, The selectivity, voltage-dependence and acid sensitivity of the tandem pore potassium channel TASK-1: Contributions of the pore domains. *Pflugers Arch.* **455**, 333–348 (2007).

58. S. Liu, P. J. Focke, K. Matulef, X. Bian, P. Moënne-Loccoz, F. I. Valiyaveetil, S. W. Lockless, Ion-binding properties of a K^+ channel selectivity filter in different conformations. *Proc. Natl. Acad. Sci. U.S.A.* **112**, 15096–15100 (2015).

59. J. Li, J. Ostmeyer, E. Boulanger, H. Rui, E. Perozo, B. Roux, Chemical substitutions in the selectivity filter of potassium channels do not rule out constricted-like conformations for C-type inactivation. *Proc. Natl. Acad. Sci. U.S.A.* **114**, 11145–11150 (2017).

60. J. Li, J. Ostmeyer, L. G. Cuello, E. Perozo, B. Roux, Rapid constriction of the selectivity filter underlies C-type inactivation in the KcsA potassium channel. *J. Gen. Physiol.* **150**, 1408–1420 (2018).

61. P. K. Devaraneni, A. G. Komarov, C. A. Costantino, J. J. Devereaux, K. Matulef, F. I. Valiyaveetil, Semisynthetic K^+ channels show that the constricted conformation of the selectivity filter is not the C-type inactivated state. *Proc. Natl. Acad. Sci. U.S.A.* **110**, 15698–15703 (2013).

62. E. A. W. van der Cruijsen, D. Nand, M. Weingarth, A. Prokofyev, S. Hornig, A. A. Cukkemane, A. M. J. J. Bonvin, S. Becker, R. E. Hulse, E. Perozo, O. Pongs, M. Baldus, Importance of lipid-pore loop interface for potassium channel structure and function. *Proc. Natl. Acad. Sci. U.S.A.* **110**, 13008–13013 (2013).

63. L. Ma, D. Roman-Campos, E. D. Austin, M. Eyries, K. S. Sampson, F. Soubrier, M. Germain, D.-A. Trégouët, A. Borczuk, E. B. Rosenzweig, B. Girerd, D. Montani, M. Humbert, J. E. Loyd, R. S. Kass, W. K. Chung, A novel channelopathy in pulmonary arterial hypertension. *N. Engl. J. Med.* **369**, 351–361 (2013).

64. S. Jekhmane, J. Medeiros-Silva, J. Li, F. Kümmerer, C. Müller-Hermes, M. Baldus, B. Roux, M. Weingarth, Shifts in the selectivity filter dynamics cause modal gating in K^+ channels. *Nat. Commun.* **10**, 123 (2019).

65. F. Maingret, I. Lauritzen, A. J. Patel, C. Heurteaux, R. Reyes, F. Lesage, M. Lazdunski, E. Honoré, TREK-1 is a heat-activated background K^+ channel. *EMBO J.* **19**, 2483–2491 (2000).

66. A. J. Patel, E. Honoré, F. Maingret, F. Lesage, M. Fink, F. Duprat, M. Lazdunski, A mammalian two pore domain mechano-gated S-like K^+ channel. *EMBO J.* **17**, 4283–4290 (1998).

67. J. Chemin, A. J. Patel, F. Duprat, I. Lauritzen, M. Lazdunski, E. Honoré, A phospholipid sensor controls mechanogating of the K^+ channel TREK-1. *EMBO J.* **24**, 44–53 (2004).

68. E. Honoré, F. Maingret, M. Lazdunski, A. J. Patel, An intracellular proton sensor commands lipid- and mechano-gating of the K^+ channel TREK-1. *EMBO J.* **21**, 2968–2976 (2002).

69. Y. Kim, H. Bang, C. Gnatenco, D. Kim, Synergistic interaction and the role of C-terminus in the activation of TRAAK K^+ channels by pressure, free fatty acids and alkali. *Pflugers Arch.* **442**, 64–72 (2001).

70. Y. Kim, C. Gnatenco, H. Bang, D. Kim, Localization of TREK-2 K^+ channel domains that regulate channel kinetics and sensitivity to pressure, fatty acids and pH_i. *Pflugers Arch.* **442**, 952–960 (2001).

71. C. McClenaghan, M. Schewe, P. Aryal, E. P. Carpenter, T. Baukrowitz, S. J. Tucker, Polymodal activation of the TREK-2 K2P channel produces structurally distinct open states. *J. Gen. Physiol.* **147**, 497–505 (2016).

72. C. Heurteaux, N. Guy, C. Laigle, N. Blondeau, F. Duprat, M. Mazzuca, L. Lang-Lazdunski, C. Widmann, M. Zanzouri, G. Romey, M. Lazdunski, TREK-1, a K^+ channel involved in neuroprotection and general anesthesia. *EMBO J.* **23**, 2684–2695 (2004).

73. R. M. Lazarenko, M. G. Fortuna, Y. Shi, D. K. Mulkey, A. C. Takakura, T. S. Moreira, P. G. Guyenet, D. A. Bayliss, Anesthetic activation of central respiratory chemoreceptor neurons involves inhibition of a THIK-1-like background K^+ current. *J. Neurosci.* **30**, 9324–9334 (2010).

74. A. Alloui, K. Zimmermann, J. Mamet, F. Duprat, J. Noël, J. Chemin, N. Guy, N. Blondeau, N. Voilley, C. Rubat-Coudert, M. Borsotto, G. Romey, C. Heurteaux, P. Reeh, A. Eschalier, M. Lazdunski, TREK-1, a K^+ channel involved in polymodal pain perception. *EMBO J.* **25**, 2368–2376 (2006).

75. M. Devilliers, J. Busserolles, S. Lolignier, E. Deval, V. Pereira, A. Alloui, M. Christin, B. Mazet, P. Delmas, J. Noel, M. Lazdunski, A. Eschalier, Activation of TREK-1 by morphine results in analgesia without adverse side effects. *Nat. Commun.* **4**, 2941 (2013).

76. D. Vivier, I. B. Soussia, N. Rodrigues, S. Lolignier, M. Devilliers, F. C. Chatelain, L. Prival, E. Chapuy, G. Bourdier, K. Bennis, F. Lesage, A. Eschalier, J. Busserolles, S. Ducki, Development of the first two-pore domain potassium channel TWIK-related K^+ channel 1-selective agonist possessing in vivo antinociceptive activity. *J. Med. Chem.* **60**, 1076–1088 (2017).

77. N. Decher, B. Ortiz-Bonnin, C. Friedrich, M. Schewe, A. K. Kiper, S. Rinné, G. Seemann, R. Peyronnet, S. Zumhagen, D. Bustos, J. Kockskämper, P. Kohl, S. Just, W. González, T. Baukrowitz, B. Stallmeyer, E. Schulze-Bahr, Sodium permeable and "hypersensitive" TREK-1 channels cause ventricular tachycardia. *EMBO Mol. Med.* **9**, 403–414 (2017).

78. X. Wu, Y. Liu, X. Chen, Q. Sun, R. Tang, W. Wang, Z. Yu, M. Xie, Involvement of TREK-1 activity in astrocyte function and neuroprotection under simulated ischemia conditions. *J. Mol. Neurosci.* **49**, 499–506 (2013).

79. W. Kabsch, Xds. *Acta Crystallogr. D Biol. Crystallogr.* **66**, 125–132 (2010).

80. P. R. Evans, G. N. Murshudov, How good are my data and what is the resolution?. *Acta Crystallogr. D Biol. Crystallogr.* **69**, 1204–1214 (2013).

81. P. A. Karplus, K. Diederichs, Assessing and maximizing data quality in macromolecular crystallography. *Curr. Opin. Struct. Biol.* **34**, 60–68 (2015).

82. P. Emsley, K. Cowtan, Coot: Model-building tools for molecular graphics. *Acta Crystallogr. D Biol. Crystallogr.* **60**, 2126–2132 (2004).

83. Collaborative Computational Project, Number 4, The CCP4 suite: Programs for protein crystallography. *Acta Crystallogr. D Biol. Crystallogr.* **50**, 760–763 (1994).

84. P. D. Adams, P. V. Afonine, G. Bunkóczi, V. B. Chen, I. W. Davis, N. Echols, J. J. Headd, L.-W. Hung, G. J. Kapral, R. W. Grosse-Kunstleve, A. J. McCoy, N. W. Moriarty, R. Oeffner, R. J. Read, D. C. Richardson, J. S. Richardson, T. C. Terwilliger, P. H. Zwart, PHENIX: A comprehensive Python-based system for macromolecular structure solution. *Acta Crystallogr. D Biol. Crystallogr.* **66**, 213–221 (2010).

85. O. S. Smart, T. O. Womack, C. Flensburg, P. Keller, W. Paciorek, A. Sharff, C. Vonrhein, G. Bricogne, Exploiting structure similarity in refinement: Automated NCS and target-structure restraints in BUSTER. *Acta Crystallogr. D Biol. Crystallogr.* **68**, 368–380 (2012).

86. A. Thorn, G. M. Sheldrick, ANODE: Anomalous and heavy-atom density calculation. *J. Appl. Cryst.* **44**, 1285–1287 (2011).

87. P. S. Huang, Y.-E. A. Ban, F. Richter, I. Andre, R. Vernon, W. R. Schief, D. Baker, RosettaRemodel: A generalized framework for flexible backbone protein design. *PLOS ONE* **6**, e24109 (2011).

88. S. Jo, T. Kim, W. Im, Automated builder and database of protein/membrane complexes for molecular dynamics simulations. *PLOS ONE* **2**, e880 (2007).

89. J. Huang, S. Rauscher, G. Nawrocki, T. Ran, M. Feig, B. L. de Groot, H. Grubmüller, A. D. MacKerell Jr., CHARMM36m: An improved force field for folded and intrinsically disordered proteins. *Nat. Methods* **14**, 71–73 (2017).

90. J. B. Klauda, R. M. Venable, J. A. Freites, J. W. O'Connor, D. J. Tobias, C. Mondragon-Ramirez, I. Vorobyov, A. D. MacKerell Jr., R. W. Pastor, Update of the CHARMM all-atom additive force field for lipids: Validation on six lipid types. *J. Phys. Chem. B* **114**, 7830–7843 (2010).

91. W. L. Jorgensen, J. Chandrasekhar, J. D. Madura, R. W. Impey, M. L. Klein, Comparison of simple potential functions for simulating liquid water. *J. Chem. Phys.* **79**, 926–935 (1983).

92. K. Vanommeslaeghe, E. Hatcher, C. Acharya, S. Kundu, S. Zhong, J. Shim, E. Darian, O. Guvench, P. Lopes, I. Vorobyov, A. D. Mackerell Jr., CHARMM general force field: A force field for drug-like molecules compatible with the CHARMM all-atom additive biological force fields. *J. Comput. Chem.* **31**, 671–690 (2010).

93. K. Vanommeslaeghe, A. D. MacKerell Jr., Automation of the CHARMM General Force Field (CGenFF) I: Bond perception and atom typing. *J. Chem. Inf. Model.* **52**, 3144–3154 (2012).

94. K. Vanommeslaeghe, E. P. Raman, A. D. MacKerell Jr., Automation of the CHARMM General Force Field (CGenFF) II: Assignment of bonded parameters and partial atomic charges. *J. Chem. Inf. Model.* **52**, 3155–3168 (2012).

95. D. Beglov, B. Roux, Finite representation of an infinite bulk system: Solvent boundary potential for computer simulations. *J. Chem. Phys.* **100**, 9050–9063 (1994).

96. D. E. Shaw, J. P. Grossman, J. A. Bank, B. Batson, J. A. Butts, J. C. Chao, M. M. Deneroff, R. O. Dror, A. Even, C. H. Fenton, A. Forte, J. Gagliardo, G. Gill, B. Greskamp, C. R. Ho, D. J. Ierardi, L. Iserovich, J. S. Kuskin, R. H. Larson, T. Layman, L.-S. Lee, A. K. Lerer, C. Li, D. Killebrew, K. M. Mackenzie, S. Y.-H. Mok, M. A. Moraes, R. Mueller, L. J. Nociolo, J. L. Peticolas, T. Quan, D. Ramot, J. K. Salmon, D. P. Scarpazza, U. B. Schafer, N. Siddique, C. W. Snyder, J. Spengler, P. T.

P. Tang, M. Theobald, H. Toma, B. Towles, B. Vitale, S. C. Wang, C. Young, Anton 2: Raising the bar for performance and programmability in a special-purpose molecular dynamics supercomputer, in *Proceedings of the International Conference for High Performance Computing, Networking, Storage and Analysis* (*SC '14*) (IEEE, 2014), pp. 41–53.

97. M. J. Abraham, T. Murtola, R. Schulz, S. Páll, J. C. Smith, B. Hess, E. Lindahl, GROMACS: High performance molecular simulations through multi-level parallelism from laptops to supercomputers. *SoftwareX* **1-2**, 19–25 (2015).

98. J. Gumbart, F. Khalili-Araghi, M. Sotomayor, B. Roux, Constant electric field simulations of the membrane potential illustrated with simple systems. *Biochim. Biophys. Acta* **1818**, 294–302 (2012).

99. J. C. Phillips, R. Braun, W. Wang, J. Gumbart, E. Tajkhorshid, E. Villa, C. Chipot, R. D. Skeel, L. Kalé, K. Schulten, Scalable molecular dynamics with NAMD. *J. Comput. Chem.* **26**, 1781–1802 (2005).

100. G. J. Martyna, D. J. Tobias, M. L. Klein, Constant-pressure molecular-dynamics algorithms. *J. Chem. Phys.* **101**, 4177–4189 (1994).

101. S. Nosé, A molecular dynamics method for simulations in the canonical ensemble. *Mol. Phys.* **52**, 255–268 (1984).

102. W. G. Hoover, Canonical dynamics: Equilibrium phase-space distributions. *Phys. Rev. A* **31**, 1695–1697 (1985).

103. Y. Shan, J. L. Klepeis, M. P. Eastwood, R. O. Dror, D. E. Shaw, Gaussian split Ewald: A fast Ewald mesh method for molecular simulation. *J. Chem. Phys.* **122**, 054101 (2005).

104. J.-P. Ryckaert, G. Ciccotti, H. J. C. Berendsen, Numerical integration of the cartesian equations of motion of a system with constraints: Molecular dynamics of *n*-alkanes. *J. Comput. Phys.* **23**, 327–341 (1977).

105. M. Parrinello, A. Rahman, Polymorphic transitions in single-crystals: A new molecular-dynamics method. *J. Appl. Phys.* **52**, 7182–7190 (1981).

106. S. Nosé, M. L. Klein, Constant pressure molecular-dynamics for molecular systems. *Mol. Phys.* **50**, 1055–1076 (2006).

107. T. Darden, D. York, L. Pedersen, Particle mesh Ewald: An N·log(N) method for Ewald sums in large systems. *J. Chem. Phys.* **98**, 10089–10092 (1993).

108. B. Hess, H. Bekker, H. J. C. Berendsen, J. G. E. M. Fraaije, LINCS: A linear constraint solver for molecular simulations. *J. Comput. Chem.* **18**, 1463–1472 (1997).

109. N. Michaud-Agrawal, E. J. Denning, T. B. Woolf, O. Beckstein, MDAnalysis: A toolkit for the analysis of molecular dynamics simulations. *J. Comput. Chem.* **32**, 2319–2327 (2011).

110. H. Guizouarn, N. Gabillat, R. Motais, F. Borgese, Multiple transport functions of a red blood cell anion exchanger, tAE1: Its role in cell volume regulation. *J. Physiol.* **535**, 497–506 (2001).